Ceramics International 45 [5] 5276-5283 (2019)
DOI: 10.1016/j.ceramint.2018.11.225

Combination of structural and microstructural effects in the multiferroic response of Nd and Ti co-doped $BiFeO_3$ bulk ceramics

C. Gumiel,[1] T. Jardiel,[2] M.S. Bernardo,[1,2] P.G. Villanueva,[2] U. Urdiroz,[3] F. Cebollada,[1] C. Aragó,[4] A.C. Caballero,[2] M .Peiteado[1,2]

[1]POEMMA-CEMDATIC, ETSI Telecomunicación (UPM), Avd. Complutense 30, 28040 Madrid, Spain
[2]Department of Electroceramics, Instituto de Cerámica y Vidrio (CSIC), Kelsen 5, 28049 Madrid, Spain
[3]Department of Nanostructures and Surfaces, Instituto de Ciencia de Materiales de Madrid (CSIC), Sor Juana Inés de la Cruz 3, Madrid, Spain
[4]Department of Materials Physics, Facultad de Ciencias C-4 UAM, Madrid, Spain

Abstract

Different dopant strategies are currently under investigation in order to overcome the many problems that limit the commercial viability of $BiFeO_3$-based ceramic devices. Neodymium substitution onto the A site of the perovskite lattice provokes significant changes in the crystal structure of the parent material which can derive in enhanced multiferroic properties, but the conductivity in the bulk system is still too high. Titanium doping on the other hand generates a distinctive micro-nanostructure in the consolidated ceramics which can largely increase the dc resistivity of the whole material. A combination of these two effects is here attempted in a co-doping approach which evidences that the microstructural effect caused upon Ti-doping, provoking a reduction of the leakage currents, eventually allows the co-doped material to capitalize on the unique piezoelectric and magnetic properties structurally triggered by the Nd-doping.

Keywords: $BiFeO_3$; rare-earth doping; *R3*c to *Pbam* transition; rhombohedral distortion; piezoelectric and magnetic properties.

Corresponding author email address: c.gumiel@upm.es

1. Introduction

$BiFeO_3$ (BFO) is well-known to be a promising multiferroic material due to its high phase-transition temperatures, which are 645 K for the antiferromagnetic to paramagnetic transition ($T_{Néel}$) and 1103 K for the ferroelectric to paraelectric transition (T_{Curie}) [1], what could makes it able to exhibit ferroelectricity and ferromagnetism at room temperature. Both properties directly derive from a perovskite-like structure that at atmospheric pressure and room temperature presents a rhombohedrically distorted perovskite structure belonging to the *R3c* group [1,2]. However, BFO materials present several drawbacks mainly related to three different aspects. The first one would be the difficulty in obtaining this material free of secondary phases [3]. The second one is related to a weak electric response, and this includes a low remnant polarization, a high coercive field, a low dielectric constant, low piezoelectric coefficients and, probably the most relevant from the electrical point of view, a high leakage current [4,5]. Finally the third drawback is linked to the existence of a spiral spin modulation which cancels any spontaneous net magnetization in the consolidated material [6]. In order to surmount this adverse scenario different strategies have been attempted, and among them, chemical modification of $BiFeO_3$ is recognized as a potentially useful approach [7–11]. That is for example the case of rare earth substitution onto the A site (Bi^{3+}) of the perovskite lattice, which has been shown to enhance the functional properties of BFO ceramics [4,12–15]. Specifically, it has been reported that Nd^{3+} doping can promote

significant changes in the crystal structure of parent BFO that can derive in boosted piezoelectric properties, long-range ferroelectricity and even in an enhanced magnetic response by making the spin cycloid energetically unfavorable [4,16–19]. The smaller size of the Nd^{3+} ions is behind this improved picture: 1.27 Å for the 12-fold coordinated Nd^{3+} ions *versus* 1.36 Å for Bi^{3+} in cubo-octahedral coordination [7,20], which entails a decrease in the Goldschmidt tolerance factor of the BFO perovskite lattice; this essentially enhances the relative rotation of the FeO_6 octahedra [1], and eventually a structural transition is induced from the polar rhombohedrally distorted *R3c* phase to the non-polar orthorhombically distorted *Pbam* phase isostructural with anti-polar $PbZrO_3$ structure [4,18,21]. Moreover, for Nd-doping in the range of $0.15 \leq x \leq 0.20$ the two phases coexist, for example rendering the mentioned enhancement of the piezoelectric response in an analogous way to the morphotropic phase boundary of lead zirconate titanate (PZT) ceramics [21–24]. However, despite the promising results, progress towards device applications is yet hindered by the high conductivity (leakage current) which is still difficult to avoid in the Nd-doped BFO system [21,25–27]. Since an isovalent cation is incorporated, the high leakage current can largely rely on the distortion generated in the crystal lattice, but actually, the precise mechanism behind this higher conductivity upon Nd-doping is still under discussion in the specialized literature [8, 28-29].

A possible strategy to reduce this high electrical conductivity observed in Nd-doped BFO materials could be the simultaneous incorporation of Ti^{4+}. As a donor dopant, several authors affirm that Ti-substitution into the Fe positions should reduce the concentration of oxygen vacancies by compensating for Fe^{2+} (which in turn results from the reduction of Fe^{3+}), thereby reducing the number of charge carriers [30–33]. In a

previous contribution we also attributed the reduction in conductivity upon Ti-doping to a microstructural effect: its presence generates a characteristic micro-nanostructure in the BFO bulk materials in which submicronic grains are indeed composed by internal domains of nanometric size and separated by titanium-rich areas [34]. Only a limited concentration of Ti^{4+} is incorporated into the perovskite crystal lattice and both the electrical and the magnetic properties are controlled by this microstructure: The titanium-rich interfaces behave like highly resistive layers increasing the direct-current (dc) resistivity of the whole material and, simultaneously, the nanometric structural domains, which are smaller than the spin cycloid wavelength, originate a ferromagnetic-like behavior [34].

In view of this background, the present contribution addresses the challenge of combining the effects of both dopants, i.e. the structural benefit provoked by Nd^{3+}-doping (coexistence of two phases in a crossover region) and the microstructural improvement that generates Ti^{4+} (reduced conductivity), in a clear attempt to leverage the multiferroic properties of bulk BFO ceramics. A detailed analysis is conducted to figure out the possible chemical interactions between both dopants and how this can influence the functional response of the co-doped material.

2. Experimental

Ceramic bulk samples with nominal composition $Bi_{0.85}Nd_{0.15}Fe_{0.95}Ti_{0.05}O_{3.025}$ (referenced hereafter as BNFTO) were prepared using a standard solid state reaction procedure as described elsewhere [35]. The corresponding amounts of the oxide precursors, Bi_2O_3 (Aldrich, 99.9 %), Fe_2O_3 (Sigma-Aldrich, > 99 %), Nd_2O_3 (Aldrich 99.9 %) and TiO_2 (anatase structure, Sigma-Aldrich, > 99%) were weighed and

subjected to 2 hours of attrition milling with YSZ balls and ethanol as liquid medium. The dried mixtures were sieved under a 100 μm mesh and calcined at 800 ºC during 2 hours for the synthesis process, with heating and cooling rates of 3 °C/min. The calcined powders were again milled, sieved and pressed isostatically at 250 MPa in ϕ = 0.8 cm pellets. In order to obtain the highest density and the lowest amount of secondary phases the pressed pellets were subjected to several sintered treatments, having found a density of 95 % of the $BiFeO_3$ theoretical density when sintering the samples at 925ºC/8h. For comparison issues, samples with the following nominal compositions were prepared applying similar processing conditions: $BiFeO_3$ (BFO), $BiFe_{0.95}Ti_{0.05}FeO_3$ (BFTO) and $Bi_{0.85}Nd_{0.15}FeO_3$ (BNFO). For these other materials the optimum sintering conditions (temperatures and times showing the highest density combined with lowest amount of secondary phases) were found to be 800ºC/2h for BFO, 825ºC/2h for BFTO and 925ºC/4h for BNFO. Notice that in all the doped compositions the sintering temperatures are above the peritectic point of pure BFO, but in any case this is not affecting the distribution, purity and/or stoichiometry of the crystallized phases.

The sintered ceramics were structurally characterized by means of X-ray diffraction (XRD). Patterns were collected between 2θ = 15º and 2θ = 65°, in steps of 0.015° and with a counting time of 0.5 s per step, on a Bruker D8 Advance diffractometer using CuKα radiation. The experimental data were refined using the FullProf 2k program [36] and its graphical interface WinPLOTR [37]. The densification behavior of the sintered pellets was followed by measuring the Archimedes density in water. The microstructural characterization was conducted on polished and thermally or chemically (diluted HCl) etched surfaces by Field Emission Scanning Electron Microscopy

(FESEM), using a Hitachi S-4700 microscope equipped with EDS. The electrical characterization was carried out on Ag-Pd electroded discs. Direct-current (dc) conductivity measurements were performed at 220 ºC in a voltage range between 20 V and 200 V, using a Keithley Model 2410 power multimeter. Ferroelectric loops and piezoelectric coefficients d_{31} and d_{33} were determined by respectively using a RT6000HVS hysteresimeter (Radiant technologies) and an impedance analyzer (Agilent 4294A) with the resonance–anti-resonance technique. The magnetization curves were measured using a VSM (MagLabVSM Oxford Instruments MLVSM9) at room temperature and with a magnetic field range from -6 T to +6 T. All measurements registered the change in magnetization as a function of the applied magnetic field (M vs. H).

3. Results and discussion

Figure 1 shows the X-ray diffraction patterns corresponding to the four tested compositions right after the sintering step. It should be noticed that for the structural analyses, the BFO and the BFTO pellets subjected to examination were actually sintered at a higher temperature (900ºC) than the one corresponding to their maximum density (800ºC for BFO and 825ºC for BFTO, see experimental). This was opted aiming a more accurate and thermodynamically-comparable observation of the structural differences between compositions (BNFO and BNFTO sinter at 925ºC, but this temperature was in impracticable for BFO and BFTO since induced decomposition). As observed in **Figure 1**, the undoped BFO material is largely composed by the rhombohedral *R3c* phase of $BiFeO_3$ (ICDD nº 071-2494) although some diffraction maxima can be as well ascribed to the characteristic $Bi_{25}FeO_{40}$ sillenite-type (ICDD nº 046-0416) and $Bi_2Fe_4O_9$ mullite-

type (ICDD nº 025-0090) secondary phases. The same distribution but with a slightly higher proportion of the secondary compounds is observed for the BFTO Ti-doped sample, whose diffraction pattern also evidenced a certain displacement of the $BiFeO_3$ *R3c* peaks to higher 2Θ values. But the picture drastically changes with the incorporation of neodymium, samples BNFO and BNFTO. The mullite and sillenite phases are any more detected and instead the mentioned crossover from rhombohedral *R3c* to the orthorhombic *Pbam* phase has been produced, yielding X-ray diffraction patterns in which both $BiFeO_3$ phases coexist (no ICDD card is available for the *Pbam* structure; it is indexed according to the work by Karimi *et al.* [21] and the more recent one by Walker *et al.* [38]). Interestingly, the proportion between these *R3c* and *Pbam* phases is different for the two compositions containing neodymium. **Figure 2** shows an amplified depiction of the XRD patterns of these two samples that focuses on the 2θ region between 44 and 48º. The two diffraction maxima observed in this region correspond to the *R3c* rhombohedral and the *Pbam* orthorhombic phases of $BiFeO_3$, and after running the corresponding deconvolution processes the estimation of the respective peak areas yields the following proportions: 60% *R3c* – 40% *Pbam* for the BNFO composition, and 67% *R3c* – 33% *Pbam* for the BNFTO material, i.e. a visible smaller amount of *Pbam* phase for the co-doped system. Since the *R3c* to *Pbam* phase transition is a thermally and kinetically activated episode [17,39], this result is initially inconsistent with the longer dwell time used for sintering the co-doped material, 925ºC/8h for the BNFTO sample and 925ºC/4h for BNFO. Clearly, the presence of titanium is altering the regular progression of the *R3c* to *Pbam* phase transition in the co-doped material and one plausible mechanism is described as follows: The *R3c* to *Pbam* transition involves the diffusion of the neodymium ions within the matrix of the

R3c phase and the subsequent re-crystallization of the *Pbam* phase at Nd-enriched regions (this has been confirmed by comprehensive HRTEM studies which reveal that the coexistence of the two phases occurs at the nanoscale level, with individual chemically homogeneous grains consisting of an intimate nanoscale *R3c*-*Pbam* phase mixture [22,38]). Titanium on the other hand is prone to block the diffusion processes and the overall solid state reactivity in $BiFeO_3$-based materials [34,40]. Thus, in the BNFTO co-doped sample the introduced titanium would be acting as a blocking element for the diffusion of neodymium, pinning the re-crystallization of the *Pbam* phase and leading to its lower proportion in the BNFTO sample. Simultaneously, the *R3c* phase in this Ti-doped sample would retain a higher concentration of neodymium than the *R3c* phase of the sample without Ti (BFNO). This last scenario can be corroborated by analyzing the evolution of the *R3c* lattice parameters with the composition. In doing so, a Rietveld fitting analysis was conducted for the four diffraction patterns of the sintered samples (at the indicated temperatures). The refinements are shown in **Figure 3** and the refined cell parameters are listed in **Table 1.** The obtained data indicate that the *R3c* phase retains its rhombohedral symmetry in all cases, but a different degree of incorporation is found for the two tested dopants. On one hand, no big changes in the lattice parameters and the volume cell can be observed for the material only doped with titanium, BFTO sample, suggesting a minor incorporation of Ti into the *R3c* lattice. The mentioned tendency of titanium to segregate to the grain boundaries [34], together with a predictable poor inertia of starting TiO_2 to diffuse [40], can explain such shortened incorporation of Ti. Neodymium on the other hand is more easily incorporated to the *R3c* lattice, yielding a manifest decrease of the primitive cell volume for the BNFO composition and even larger for the BNFTO co-doped sample,

see **Table 1**. In this last case, assuming the same mentioned difficulties of titanium to diffuse, that larger volume contraction of the *R3c* cell confirms that it retains a higher content of Nd, resulting for a lower amount of re-crystalized *Pbam* phase. Necessarily, these structural and compositional particularities of the BNFTO co-doped material should have an impact on its multiferroic response, as will be discussed later.

The performed XRD characterization reveals another interesting feature which this time is related to the decrease in the rhombohedral distortion of the *R3c* phase. **Figure 4** now shows the amplified 2θ region between 30 and 34º as taken again from the diffraction patterns of Figure 1. For the parent BFO material this area shows a double *hkl* reflection profile which is attributed to the *R3c* rhombohedral phase. This double *R3c* profile stays upon doping with titanium, BFTO sample. However the incorporation of neodymium makes the two Bragg peaks of the *R3c* phase to converge into a single *hkl* reflection, coinciding also with the entering of the *Pbam* orthorhombic phase. This circumstance is observed for the two samples doped with neodymium, BNFO and the co-doped BNFTO, and denotes that Nd-doping produces a decrease of the rhombohedral distortion of the *R3c* phase (although not implying a change of its rhombohedral symmetry as confirmed by the Rietveld fitting). A similar evolution has been previously observed when doping $BiFeO_3$ with Samarium [38] or even Barium [41] (A-site substitution), and as it will be also discussed later on, it will have an influence on the magnetic properties of the sintered materials.

Field emission scanning electron microscopy was subsequently used to investigate the microstructure of the sintered materials, now at the optimized temperature for their maximum density (with regards to the XRD analyses this only changes for the BFO and BFTO specimens, now sintered at 800ºC/2h and 825ºC/2h, respectively). **Figure 5**

shows the micrographs of the polished and thermally/chemically etched surfaces for the four sintered pellets. The parent BFO sample evidences the characteristic (in equilibrium) multiphase configuration whereby the $BiFeO_3$ matrix crystallizes together with a significant amount of the secondary $Bi_{25}FeO_{40}$ sillenite-type and $Bi_2Fe_4O_9$ mullite-type phases [3]. An average size of 5 μm is estimated for the $BiFeO_3$ grains in this undoped material, **Figure 5a**. The introduction of titanium in the BFTO formulation, **Figure 5b**, drastically reduces the size of the perovskite grains and produces the mentioned micro-nanostructure that we observed in our previous contribution [34]; specifically by means of HRTEM and EDS analyses in STEM mode, that research revealed that the sub-micronic grains in this BFTO system are actually composed by internal units on the scale of just a few tens of nanometers and separated by Ti-enriched interfaces [34]. Initially no clear evidence of secondary phases can be seen on the micrograph corresponding to this BFTO material, **Figure 5b**; however, pictures taken from the polished non-etched surface of the pellet (not shown here) display the coexistence of both the sillenite and mullite phases with $BiFeO_3$, hence agreeing with the information provided by the XRD analyses. Doping with neodymium however leads to a complete different microstructure in sample BNFO, **Figure 5c**. The presence of secondary phases is negligible (also in the non-etched-surface images) and a patent increase in the size of the perovskite grains is perceived, now with an average value around 9 μm; this indicates that opposite to the grain growth inhibiting role of titanium, the presence of neodymium allows for a better diffusion of mater during the consolidation of the ceramic powder. But visibly, the most significant result from these microstructural observations is the one inferred from the micrograph of the BNFTO co-doped material, **Figure 5d**. When the two dopants are jointly added to the starting

formulation, the microstructural development induced by the presence of titanium is prevailing, leading virtually to the same microstructure that is observed for the BFTO material with a restrained growth of the $BiFeO_3$ grains. This can be interpreted as follows: like in the BFTO system, in the BFTNO co-doped material the incorporated Titanium preferentially locates at the grain boundaries and just a minor amount enters the perovskite lattice. This asymmetry results in a retarding force or *drag* on the boundary which reduces the driving force for migration and inhibits the grain growth.[42] The addition of Nd, a grain growth promoter, increases the driving force for the mass transport, but still not sufficiently to overcome the solute drag effect provoked by Ti. Thus, in terms of grain growth, the BNFTO sample practically behaves as the BFTO material. The main difference between both microstructures is then compositional and results from the presence of Nd: complementary EDS analyses throughout the co-doped pellet revealed no explicit chemical interactions between Ti and Nd in terms of the formation of intermediate phases, thick interfaces or isolated clusters, so we can also presume that in this BNFTO sample the added neodymium is fairly incorporated inside the (Ti-enclosed) $BiFeO_3$ nanometric domains, where it would be steering the described structural crossover between the *R3c* and the *Pbam* phases.

Evolution of the multiferroic properties

The leakage current was evaluated by *dc* conductivity measurements registering current density as a function of the applied electric field, as it is shown in **Figure 6**. Since an almost-linear behavior was observed in the working range for all the measured materials, ohmic conduction was presumed and the *dc* resistivity values were estimated from the slope of the straight line obtained by a least-squares fit of the measurements.

This renders resistivity values in the range of 10^5 Ω·cm for the BFO sample, 10^6 Ω·cm for BNFO and around 10^7 Ω·cm for the two materials containing titanium, the BFTO and the co-doped BNFTO samples. The results confirm that Ti-doping is effective at reducing the leakage currents in $BiFeO_3$, and this effect extends to the sample co-doped with neodymium. As mentioned in the introduction, several mechanisms have been posted in the literature that may explain the observed decrease in conductivity upon Ti-doping, including the compensation of Ti^{4+} for Fe^{2+} and the subsequent elimination of oxygen vacancies, the formation of bismuth vacancies and even the formation of defect complexes [30–33,43]. For the Ti,Nd co-doped system it has been also suggested that the formation of neodymium vacancies and the local precipitation of NdO_x nanorods that compensate for the Ti substitution onto Fe sites, can also lower the electrical conductivity of the material [44]. Not declining any of these possibilities, our experiments suggest that the observed reduction in the conductivity can be further determined by the attained microstructure (Figures 5b and 5d): the resulting Ti-rich [34] inner grain boundaries, behaving as insulating barriers, constitute a highly resistive interconnected skeleton which controls the macroscopic conductivity of the material.

The ferroelectric characterization of the sintered samples was next attempted by means of polarization vs. electric field measurements. It is actually a challenging task for this kind of bulk materials since the combination of high leakage currents with large coercive fields usually impedes for reaching a saturated polarization. In our case, the decrease of the leakage current upon Ti-doping allowed the registering of some response for the BFTO and BNFTO samples, but still the corresponding P-E hysteresis loops were far from saturation and render no printable result. The situation however changed when evaluating the piezoelectric response. After different approaches both Ti-

doped pellets were effectively poled at 50 kV/cm and 100 ºC (again the high leakage currents impeded the poling of the BFO and BNFO samples without titanium) and the macroscopic piezoelectric response was assessed by the resonance-antiresonance method. The obtained results were conclusive: whereas no piezoelectric coefficients could be measured for the BFTO sample, a d_{31} of ca. $7 \cdot 10^{-12}$ C/N and a d_{33} of ca. $10 \cdot 10^{-12}$ C/N were estimated for the BNFTO sample, see **Figure 7**. Such an extensive macroscopic piezoelectric performance is difficult to obtain in $BiFeO_3$ bulk ceramics, and only a similar piezoelectric activity has been recently observed in mechanochemically activated samarium-doped $BiFeO_3$ samples (when poled in analogous conditions) [45]. In a recent report by Xu and co-workers, it has been remarked that the only way to obtain an enhancement of the d_{33} in the RE-doped $BiFeO_3$ system is if several phases coexist (likely in the form of domains), giving place to what can be called a discontinuous morphotropic phase boundary [17]. In our case, that is the role to be played by the *R3c* and *Pbam* phases of $BiFeO_3$ that we observe upon Nd-doping, but obviously, this role only be exploited if the material also exhibits a low conductivity like the one attained with the titanium co-doping.

Finally the effect of Nd^{3+} and Ti^{4+} co-doping in the magnetic properties of the bulk bismuth ferrite ceramics was also studied. **Figure 8a** first shows the room temperature magnetization curves for the BFO and the BFTO samples, whose magnetic behavior has been previously reported in the literature [5,34,46]. The parent BFO sample shows an almost-linear relationship between the magnetic field and the magnetization, the expected behavior for an antiferromagnet below T_N. A hysteresis loop is observed instead for the Ti-doped material, BFTO sample, which in addition to the linear component displays a ferromagnetic-like contribution. Specifically, the introduction of

titanium is leading to a remnant magnetization of 0.155 emu/g and a coercive field of 1.198 Tesla, see **Table 2**. The distinctive micro-nanostructure obtained upon Ti-doping is behind this improved magnetic behavior, with the nanometric structural domains leading to a rupture of the spin cycloid which results in a frustrated antiferromagnetic response. Moreover, the small size of the grains might further help to increase the coercivity values, making necessary the application of very large fields to provoke the spin orientation. **Figure 8b** then shows the corresponding magnetization curves for the BNFO and the BNFTO doped compositions. The main parameters extracted from these plots are also depicted in **Table 2**. As observed, doping with neodymium also leads to magnetic hysteresis in the BNFO sample, although in a slightly different fashion that the one produced with titanium: the remnant magnetization increases to 0.197 emu/g, whereas the coercive field stays in 0.452 Tesla. The XRD characterization of this sample revealed a mixture of *R3c* and *Pbam* $BiFeO_3$ phases (Figure 1) and initially both could have an influence on the material´s magnetic response. The *Pbam* phase is not easy to obtain as a pure single-phase and the few papers which claim to achieve it, indicate a G-type antiferromagnetic behavior for this *Pbam* orthorhombic structure [47,48]. Nevertheless, since this is yet an open debate, in this study we have considered that the main contribution to the magnetic properties of our samples is the one related to the structural changes of the *R3c* phase, specifically in a process which is related to the decrease of the rhombohedral distortion of the *R3c* phase: the incorporation of the smaller Nd^{3+} ions leads to a contraction of the unit cell by mainly lowering the c parameter (see Table 1), and this goes together with an expansion of the Fe-O-Fe bond angle [41,49,50]; the Fe-O-Fe superexchange interaction is sensitive to bond angles (and distances), and eventually the spin spiral modulation is suppressed [51] releasing

the locked magnetization of the material. This explains the enhancement of magnetization in the BFNO material as compared to the BFTO composition (table 2); on the other hand the big size of the grains of this BNFO sample (Figure 5) can further explain why this composition registers a lower coercive field than the BFTO composition. Lastly, when the two dopants are introduced in the starting formulation, BNFTO composition, the magnetic properties visibly return the combination of both effects. The remnant magnetization is even higher than in the BNFO pellet, 0.271 emu/g, which is mainly related to a structural condition: as discussed above, the BNFTO sample has a lower rhombohedral distortion (higher contraction and lower c parameter), a higher percentage of *R3c* phase and a higher content of Nd in this rhombohedral phase. This is actually in agreement with topical reports which show that the higher the amount of the rare earth entering the *R3c* lattice, the higher the suppression of the spin cycloid (it may not be completely destroyed) [49,50] and consequently the higher the released magnetization. The coercive field on the other hand shows the same amplitude (table 2) than that of the BFTO sample, also in agreement with the displayed micro-nanostructure caused by Ti-doping in this BNFTO co-doped material, see Figure 5.

Conclusions

The concurrent doping of $BiFeO_3$ with neodymium and titanium returns a remarkable improvement of the multiferroic possibilities of the bulk ceramics. No explicit chemical interactions between both dopants are ever found and so the co-doped material capitalizes on the structural and microstructural benefits provided by each element. Nd-doping induces a structural transition of the parent perovskite lattice which leads to the

coexistence of two $BiFeO_3$ phases in a crossover region. This scenario, resembling that of the morphotropic phase boundary of PZT ceramics, may render a large piezoelectric response. Additionally, the smaller Nd^{3+} ions produce a substitution-induced suppression of the spiral spin modulation which can release the locked magnetization of the material. However this proclaimed enhancement of the electromechanical and the magnetic properties of $BiFeO_3$ can only be exploited if the system is simultaneous doped with titanium, otherwise the macroscopic conductivity in the material is too high for practical applications. Ti-doping brings a confined microstructure in which nanometric domains with smaller size than the spin cycloid wavelength are embedded in a highly resistive interconnected Ti-rich skeleton that controls the macroscopic conductivity of the material. In the co-doped system neodymium is fairly incorporated inside these nanograins, where it would be steering the described structural crossover between the *R3c* and the *Pbam* phases. The resulting co-doped material displays an effective macroscopic piezoresponse and an improved ferromagnetic behavior which is not easy to attain in $BiFeO_3$ bulk ceramics.

Acknowledgments

This work has been conducted in the frame of MAT2016-80182-R and MAT2014-59210-JIN research projects.

References

[1] G. Catalan, J.F. Scott, Physics and Applications of Bismuth Ferrite, Adv. Mater. 21 (2009) 2463–2485. doi:10.1002/adma.200802849.

[2] Z. V. Gareeva, O. Diéguez, J. Íñiguez, A.K. Zvezdin, Interplay between elasticity, ferroelectricity and magnetism at the domain walls of bismuth ferrite, Phys. Status Solidi - Rapid Res. Lett. 10 (2016) 209–217. doi:10.1002/pssr.201510273.

[3] M.S. Bernardo, T. Jardiel, M. Peiteado, A.C. Caballero, M. Villegas, Reaction pathways in the solid state synthesis of multiferroic $BiFeO_3$, J. Eur. Ceram. Soc. 31 (2011) 3047–3053. doi:10.1016/j.jeurceramsoc.2011.03.018.

[4] D. Arnold, Composition-driven structural phase transitions in rare-earth-doped bifeo3 ceramics: a review, IEEE Trans. Ultrason. Ferroelectr. Freq. Control. 62 (2015) 62–82. doi:10.1109/TUFFC.2014.006668.

[5] T. Rojac, A. Bencan, B. Malic, G. Tutuncu, J.L. Jones, J.E. Daniels, D. Damjanovic, $BiFeO_3$ Ceramics: Processing, Electrical, and Electromechanical Properties, J. Am. Ceram. Soc. 97 (2014) 1993–2011. doi:10.1111/jace.12982.

[6] V.A. Khomchenko, L.C.J. Pereira, J.A. Paixão, Weak ferromagnetism and nanodimensional ferroelectric domain structure stabilized in the polar phase of $Bi_{1-x}Nd_xFeO_3$ multiferroics via Ti doping, J. Appl. Phys. 115 (2014) 164101. doi:10.1063/1.4873121.

[7] C.-H. Yang, D. Kan, I. Takeuchi, V. Nagarajan, J. Seidel, Doping $BiFeO_3$: approaches and enhanced functionality, Phys. Chem. Chem. Phys. 14 (2012) 15953. doi:10.1039/c2cp43082g.

[8] V.A. Khomchenko, D.A. Kiselev, M. Kopcewicz, M. Maglione, V.V. Shvartsman, P. Borisov, W. Kleemann, A.M.L. Lopes, Y.G. Pogorelov, J.P. Araujo, R.M. Rubinger, N.A. Sobolev, J.M. Vieira, A.L. Kholkin, Doping strategies for increased performance in $BiFeO_3$, J. Magn. Magn. Mater. 321 (2009) 1692–1698. doi:10.1016/j.jmmm.2009.02.008.

[9] M.S. Bernardo, T. Jardiel, M. Peiteado, A.C. Caballero, M. Villegas, Sintering and microstuctural characterization of W^{6+}, Nb^{5+} and Ti^{4+} iron-substituted

$BiFeO_3$, J. Alloys Compd. 509 (2011) 7290–7296. doi:10.1016/j.jallcom.2011.04.087.

[10] C. Gumiel, T. Vranken, M.S. Bernardo, T. Jardiel, A. Hardy, M.K. Van Bael, M. Peiteado, Thin film composites in the $BiFeO_3$–$Bi_4Ti_3O_{12}$ system obtained by an aqueous solution-gel deposition methodology, Bol. Soc. Esp. Ceram. V. 57 (2018) 19–28. doi:10.1016/j.bsecv.2017.09.001.

[11] Z.M. Tian, C.H. Wang, S.L. Yuan, M.S. Wu, Z.Z. Ma, H.N. Duan, L. Chen, Coexistence of room temperature ferroelectricity and ferrimagnetism in multiferroic $BiFeO_3$–$Bi_{0.5}Na_{0.5}TiO_3$ solid solution, J. Alloys Compd. 509 (2011) 8144–8148. doi:10.1016/j.jallcom.2011.05.083.

[12] J. Walker, H. Ursic, A. Bencan, B. Malic, H. Simons, I. Reaney, G. Viola, V. Nagarajan, T. Rojac, Temperature dependent piezoelectric response and strain–electric-field hysteresis of rare-earth modified bismuth ferrite ceramics, J. Mater. Chem. C. 4 (2016) 7859–7868. doi:10.1039/C6TC02000C.

[13] D. Kan, C.J. Long, C. Steinmetz, S.E. Lofland, I. Takeuchi, Combinatorial search of structural transitions: Systematic investigation of morphotropic phase boundaries in chemically substituted $BiFeO_3$, J. Mater. Res. 27 (2012) 2691–2704. doi:10.1557/jmr.2012.314.

[14] D. Kan, L. Pálová, V. Anbusathaiah, C.J. Cheng, S. Fujino, V. Nagarajan, K.M. Rabe, I. Takeuchi, Universal Behavior and Electric-Field-Induced Structural Transition in Rare-Earth-Substituted $BiFeO_3$, Adv. Funct. Mater. 20 (2010) 1108–1115. doi:10.1002/adfm.200902017.

[15] D. Wang, M. Wang, F. Liu, Y. Cui, Q. Zhao, H. Sun, H. Jin, M. Cao, Sol–gel synthesis of Nd-doped $BiFeO_3$ multiferroic and its characterization, Ceram. Int. 41 (2015) 8768–8772. doi:10.1016/j.ceramint.2015.03.100.

[16] L. Jin, W.B. Luo, X. Qing, Y. Shuai, C. Yang, C.G. Wu, W.L. Zhang, Nd doping effects on the multifunction properties of $BiFeO_3$, Mater. Res. Innov. 19 (2015) s35–s39. doi:10.1179/1432891715Z.0000000002049.

[17] B. Xu, D. Wang, J. Íñiguez, L. Bellaiche, Finite-Temperature Properties of Rare-Earth-Substituted $BiFeO_3$ Multiferroic Solid Solutions, Adv. Funct. Mater. 25 (2015) 552–558. doi:10.1002/adfm.201403811.

[18] C.-S. Tu, P.-Y. Chen, C.-S. Chen, C.-Y. Lin, V.H. Schmidt, Tailoring microstructure and photovoltaic effect in multiferroic Nd-substituted $BiFeO_3$ ceramics by processing atmosphere modification, J. Eur. Ceram. Soc. 38 (2018) 1389–1398. doi:10.1016/j.jeurceramsoc.2017.11.025.

[19] S. Pu, H. Zheng, Z. Chen, M. Li, Z. Hu, J. Wang, H. Zou, The microstructure and ferroelectric property of Nd-doped multiferroic ceramics $Bi_{0.85}Nd_{0.15}FeO_3$, Ceram. Int. 41 (2015) 5498–5504. doi:10.1016/j.ceramint.2014.12.121.

[20] Y.Q. Jia, Crystal radii and effective ionic radii of the rare earth ions, J. Solid State Chem. 95 (1991) 184–187. doi:10.1016/0022-4596(91)90388-X.

[21] S. Karimi, I.M. Reaney, Y. Han, J. Pokorny, I. Sterianou, Crystal chemistry and domain structure of rare-earth doped $BiFeO_3$ ceramics, J. Mater. Sci. 44 (2009) 5102–5112. doi:10.1007/s10853-009-3545-1.

[22] T. Wang, T. Xu, S. Gao, S.H. Song, Effect of Nd and Nb co-doping on the structural, magnetic and optical properties of multiferroic $BiFeO_3$ nanoparticles prepared by sol-gel method, Ceram. Int. 43 (2017) 4489–4495. doi:10.1016/j.ceramint.2016.12.100.

[23] C.R. Foschini, M.A. Ramirez, S.R. Simões, J.A. Varela, E. Longo, A.Z. Simões, Piezoresponse force microscopy characterization of rare-earth doped $BiFeO_3$ thin films grown by the soft chemical method, Ceram. Int. 39 (2013) 2185–2195. doi:10.1016/j.ceramint.2012.08.083.

[24] S. Fujino, M. Murakami, V. Anbusathaiah, S.H. Lim, V. Nagarajan, C.J. Fennie, M. Wuttig, L. Salamanca-Riba, I. Takeuchi, Combinatorial discovery of a lead-free morphotropic phase boundary in a thin-film piezoelectric perovskite, Appl. Phys. Lett. 92 (2008). doi:10.1063/1.2931706.

[25] S. Karimi, I.M. Reaney, I. Levin, I. Sterianou, Nd-doped $BiFeO_3$ ceramics with antipolar order, Appl. Phys. Lett. 94 (2009) 112903. doi:10.1063/1.3097222.

[26] S. Pattanayak, R.N.P. Choudhary, Synthesis, electrical and magnetic characteristics of Nd-modified $BiFeO_3$, Ceram. Int. 41 (2015) 9403–9410. doi:10.1016/j.ceramint.2015.03.318.

[27] A. Kumar, D. Varshney, Crystal structure refinement of $Bi_{1-x}Nd_xFeO_3$ multiferroic by the Rietveld method, Ceram. Int. 38 (2012) 3935–3942. doi:10.1016/j.ceramint.2012.01.046.

[28] P. Godara, A. Agarwal, N. Ahlawat, S. Sanghi, Crystal structure refinement, dielectric and magnetic properties of Sm modified $BiFeO_3$ multiferroic, J. Mol. Struct. 1097 (2015) 207–213. doi:10.1016/j.molstruc.2015.05.022.

[29] B. Deka, S. Ravi, D. Pamu, Evolution of structural transition, grain growth inhibition and collinear antiferromagnetism in $(Bi_{1-x}Sm_x)FeO_3$ (x = 0 to 0.3) and their effects on dielectric and magnetic properties, Ceram. Int. 43 (2017) 16580–16592. doi:10.1016/j.ceramint.2017.09.046.

[30] K. Kalantari, I. Sterianou, S. Karimi, M.C. Ferrarelli, S. Miao, D.C. Sinclair, I.M. Reaney, Ti-doping to reduce conductivity in $Bi_{0.85}Nd_{0.15}FeO_3$ ceramics, Adv. Funct. Mater. 21 (2011) 3737–3743. doi:10.1002/adfm.201100191.

[31] I.M. Reaney, I. MacLaren, L. Wang, B. Schaffer, A. Craven, K. Kalantari, I. Sterianou, S. Miao, S. Karimi, D.C. Sinclair, Defect chemistry of Ti-doped antiferroelectric $Bi_{0.85}Nd_{0.15}FeO_3$, Appl. Phys. Lett. 100 (2012). doi:10.1063/1.4705431.

[32] X.H. Zheng, Z.H. Ma, P.J. Chen, D.P. Tang, N. Ma, Decomposition behavior and dielectric properties of Ti-doped $BiFeO_3$ ceramics derived from molten salt method, J. Mater. Sci. Mater. Electron. 23 (2012) 1533–1537. doi:10.1007/s10854-012-0624-x.

[33] Y. Tian, F. Xue, Q. Fu, L. Zhou, C. Wang, H. Gou, M. Zhang, Structural and physical properties of Ti-doped $BiFeO_3$ nanoceramics, Ceram. Int. 44 (2018) 4287–4291. doi:10.1016/j.ceramint.2017.12.013.

[34] M.S. Bernardo, T. Jardiel, M. Peiteado, F.J. Mompean, M. Garcia-Hernandez, M.A. Garcia, M. Villegas, A.C. Caballero, Intrinsic compositional inhomogeneities in bulk Ti-doped $BiFeO_3$: Microstructure development and

multiferroic properties, Chem. Mater. 25 (2013) 1533–1541. doi:10.1021/cm303743h.

[35] M.S. Bernardo, D.G. Calatayud, T. Jardiel, D. Makovec, M. Peiteado, A.C. Caballero, Titanium doping of $BiFeO_3$ ceramics and identification of minor phases by Raman spectroscopy, J. Raman Spectrosc. 48 (2017) 884–890. doi:10.1002/jrs.5116.

[36] J. Rodríguez-Carvajal, Recent advances in magnetic structure determination by neutron powder diffraction, Phys. B Phys. Condens. Matter. 192 (1993) 55–69. doi:10.1016/0921-4526(93)90108-I.

[37] T. Roisnel, J. Rodríquez-Carvajal, WinPLOTR: A Windows Tool for Powder Diffraction Pattern Analysis, Mater. Sci. Forum. 378-381 (2001) 118–123. doi:10.4028/www.scientific.net/MSF.378-381.118.

[38] J. Walker, H. Simons, D.O. Alikin, A.P. Turygin, V.Y. Shur, A.L. Kholkin, H. Ursic, A. Bencan, B. Malic, V. Nagarajan, T. Rojac, Dual strain mechanisms in a lead-free morphotropic phase boundary ferroelectric, Sci. Rep. 6 (2016). doi:10.1038/srep19630.

[39] O. Singh, A. Agarwal, A. Das, S. Sanghi, A. Jindal, Evolution of structural and magnetic phases in Nd doped $BiFeO_3$ multiferroics with sintering time, J. Magn. Magn. Mater. 442 (2017) 200–207. doi:10.1016/j.jmmm.2017.06.113.

[40] C. Gumiel, M.S. Bernardo, P.G. Villanueva, T. Jardiel, J. de Frutos, A.C. Caballero, M. Peiteado, Solid state diffusion and reactivity in the multiferroic $BiFeO_3$–$Bi_4Ti_3O_{12}$ composite system, J. Mater. Sci. (2016). doi:10.1007/s10853-016-0666-1.

[41] G. Rojas-George, J. Silva, R. Castañeda, D. Lardizábal, O.A. Graeve, L. Fuentes, A. Reyes-Rojas, Modifications in the rhombohedral degree of distortion and magnetic properties of Ba-doped $BiFeO_3$ as a function of synthesis methodology, Mater. Chem. Phys. 146 (2014) 73–81. doi:10.1016/j.matchemphys.2014.02.044.

[42] M.N. Rahaman, Ceramic Processing and Sintering, Marcel Dekker Inc, New York, 1995.

[43] J.H. Zhu, J.Q. Dai, J.W. Xu, X.Y. Li, Effect of Zn and Ti Co-doping on structure and electrical properties of $BiFeO_3$ ceramics, Ceram. Int. 44 (2018) 9215–9220. doi:10.1016/j.ceramint.2018.02.131.

[44] I. Maclaren, L.Q. Wang, B. Schaffer, Q.M. Ramasse, A.J. Craven, S.M. Selbach, N.A. Spaldin, S. Miao, K. Kalantari, I.M. Reaney, Novel nanorod precipitate formation in neodymium and titanium codoped bismuth ferrite, Adv. Funct. Mater. 23 (2013) 683–689. doi:10.1002/adfm.201201835.

[45] J. Walker, H. Ursic, A. Bencan, B. Malic, H. Simons, I. Reaney, G. Viola, V. Nagarajan, T. Rojac, Temperature dependent piezoelectric response and strain-electric-field hysteresis of rare-earth modified bismuth ferrite ceramics, J. Mater. Chem. C. 4 (2016) 7859–7868. doi:10.1039/c6tc02000c.

[46] M.S. Bernardo, Synthesis, microstructure and properties of $BiFeO_3$-based multiferroic materials: A review, Bol. Soc. Esp. Ceram. V. 53 (2014) 1–14. doi:10.3989/cyv.12014.

[47] I. Levin, S. Karimi, V. Provenzano, C.L. Dennis, H. Wu, T.P. Comyn, T.J. Stevenson, R.I. Smith, I.M. Reaney, Reorientation of magnetic dipoles at the antiferroelectric-paraelectric phase transition of $Bi_{1-x}Nd_xFeO_3$ ($0.15<x<0.25$), Phys. Rev. B. 81 (2010) 020103(R). doi: 10.1103/PhysRevB.81.020103.

[48] I. Levin, M.G. Tucker, H. Wu, V. Provenzano, C.L. Dennis, S. Karimi, T.P. Comyn, T.J. Stevenson, R.I. Smith, I.M. Reaney, Displacive phase transitions and magnetic structures in Nd-substituted $BiFeO_3$, Chem. Mater. 23 (2011) 2166-2175. doi:10.1021/cm1036925.

[49] P. Chandra Sati, M. Arora, S. Chauhan, M. Kumar, S. Chhoker, Effect of Dy substitution on structural, magnetic and optical properties of $BiFeO_3$ ceramics, J. Phys. Chem. Solids. 75 (2014) 105–108. doi:10.1016/j.jpcs.2013.09.003.

[50] C. Lan, Y. Jiang, S. Yang, Magnetic properties of La and (La, Zr) doped $BiFeO_3$ ceramics, J. Mater. Sci. 46 (2011) 734–738. doi:10.1007/s10853-010-4805-9.

[51] Z. Chen, Y. Wu, X. Wang, W. Jin, C. Zhu, Ferromagnetism and enhanced photocatalytic activity in Nd doped $BiFeO_3$ nanopowders, J. Mater. Sci. Mater. Electron. 26 (2015) 9929–9940. doi:10.1007/s10854-015-3669-9.

	a = b (Å)	c (Å)	V (Å^3)
BFO	5.575 (2)	13.860 (5)	373.05 (3)
BFTO	5.577 (2)	13.840 (5)	372.75 (3)
BNFO	5.576 (9)	13.78 (3)	371.2 (1)
BNFTO	5.58 (2)	13.69 (8)	368.8 (4)

Table 1. Lattice parameters and volume of the *R3c* primitive cell for the four sintered samples, as obtained from the Rietveld fitting of the corresponding XRD patterns (see Figure 3).

	M+ (emu/g)	M- (emu/g)	Hc+ (T)	Hc- (T)
BFTO	0.155	-0.158	1.198	-1.200
BNFO	0.197	-0.200	0.452	-0.437
BNFTO	0.271	-0.273	1.263	-1.254

Table 2. Remnant magnetization and coercive field values extracted from the ferromagnetic hysteresis plots of the sintered samples (BFO parent sample yielded no measurable hysteresis)

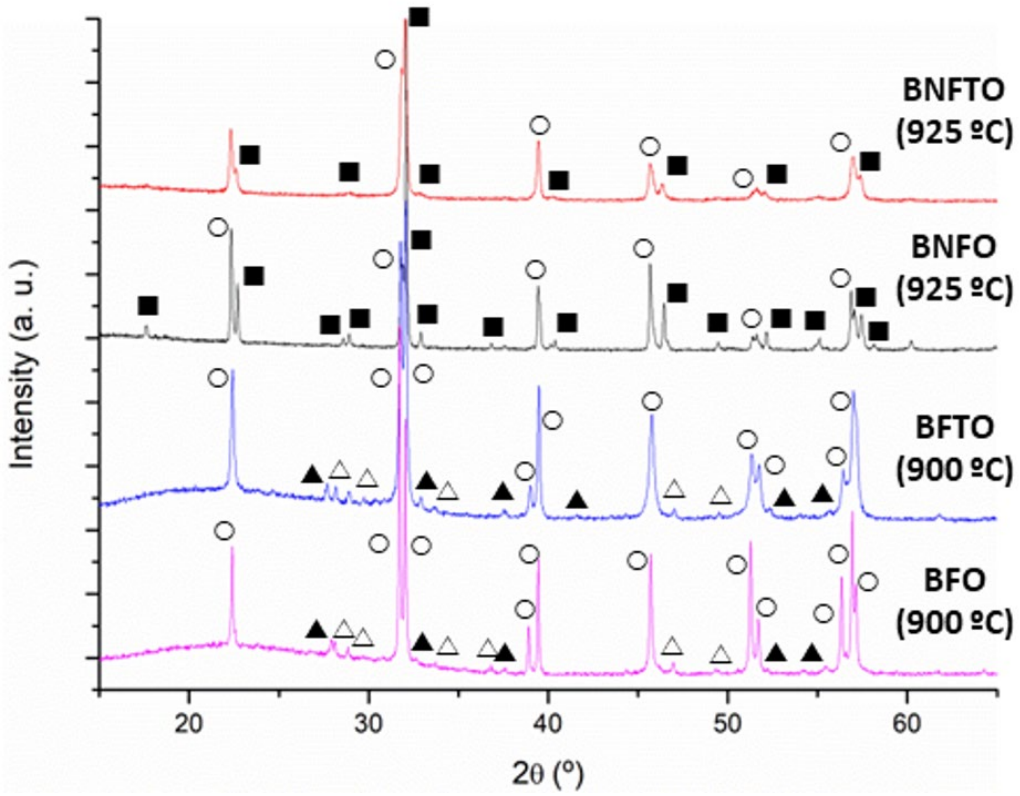

Figure 1. X-ray diffraction patterns of the sintered ceramic samples (sintering temperatures are indicated in parenthesis). White circles are assigned to the R3c $BiFeO_3$ phase, while black squares to the Pbam $BiFeO_3$ phase. The sillenite and the mullite-type phases are identified with black and white triangles, respectively.

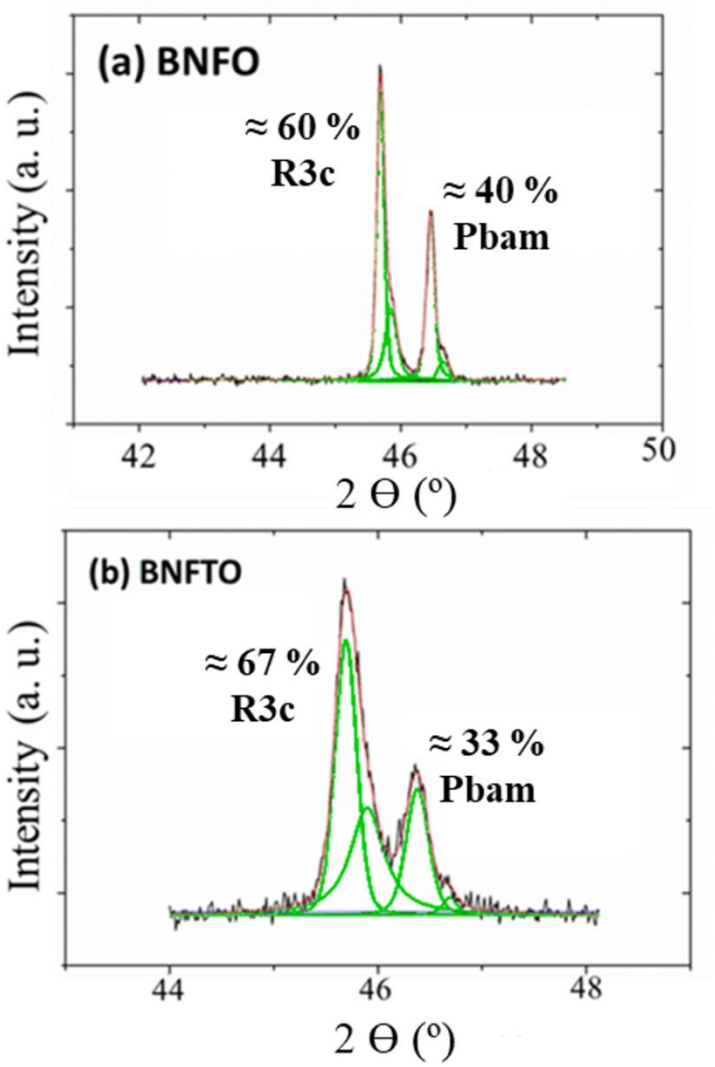

Figure 2. Amplified depiction of the X-ray diffraction patterns of the (a) BNFO and (b) BNFTO sintered samples to show the different percentage of the *R3c* and the *Pbam* phases of $BiFeO_3$, as semi-quantitatively calculated from the area of the corresponding diffraction peaks.

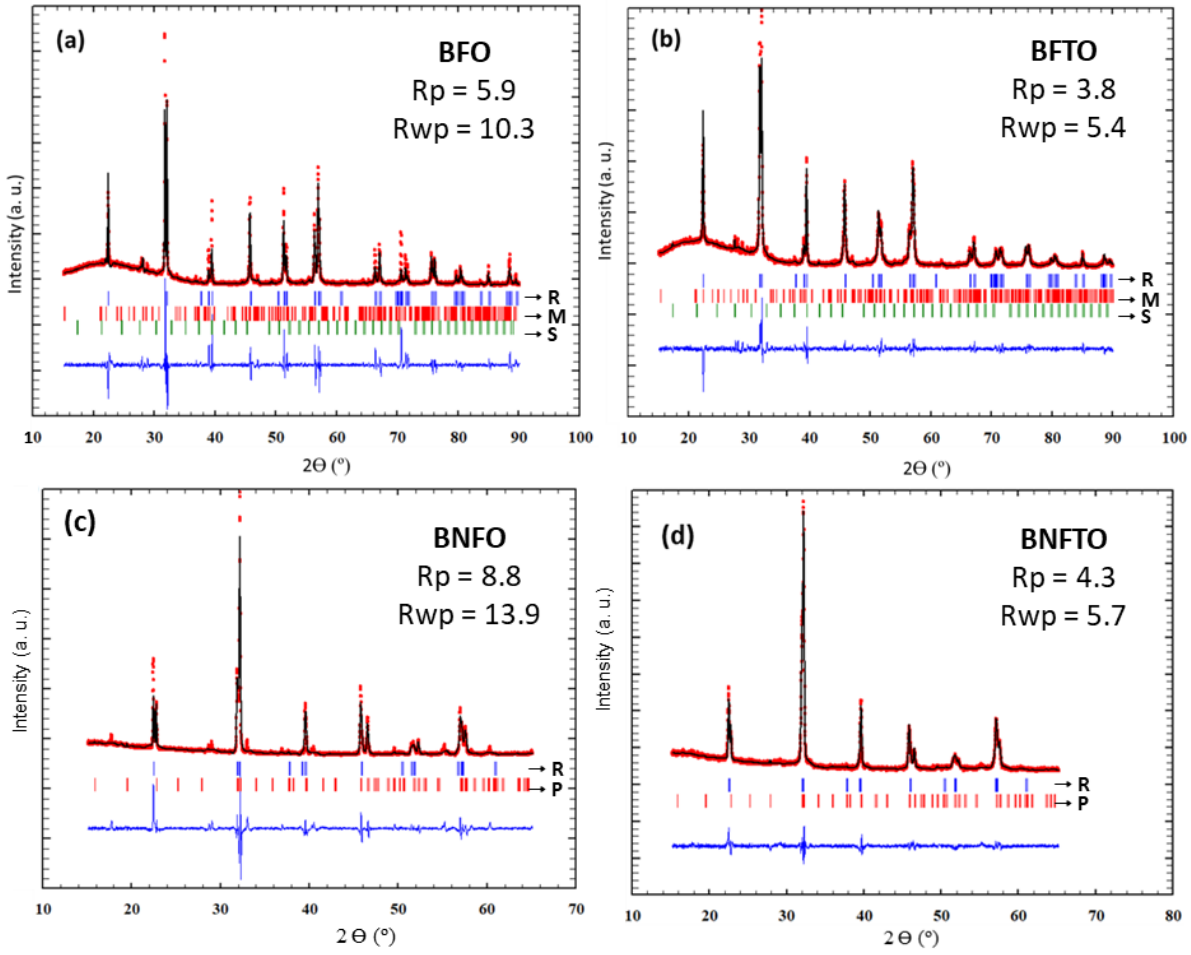

Figure 3. Rietveld refinement of the XRD patterns in Figure 1: (a) BFO sample sintered at 900 ºC/2 h, (b) BFTO sample sintered at 900 ºC/2 h, (c) BNFO sample sintered at 925 ºC/4 h and (d) BNFTO sample sintered at 925 ºC/8 h. The crystalline phases used for the corresponding refinements are labelled as: R ($BiFeO_3$ *R3c*), M ($Bi_2Fe_4O_9$), S ($Bi_{25}FeO_{40}$) and P ($BiFeO_3$ *Pbam*).

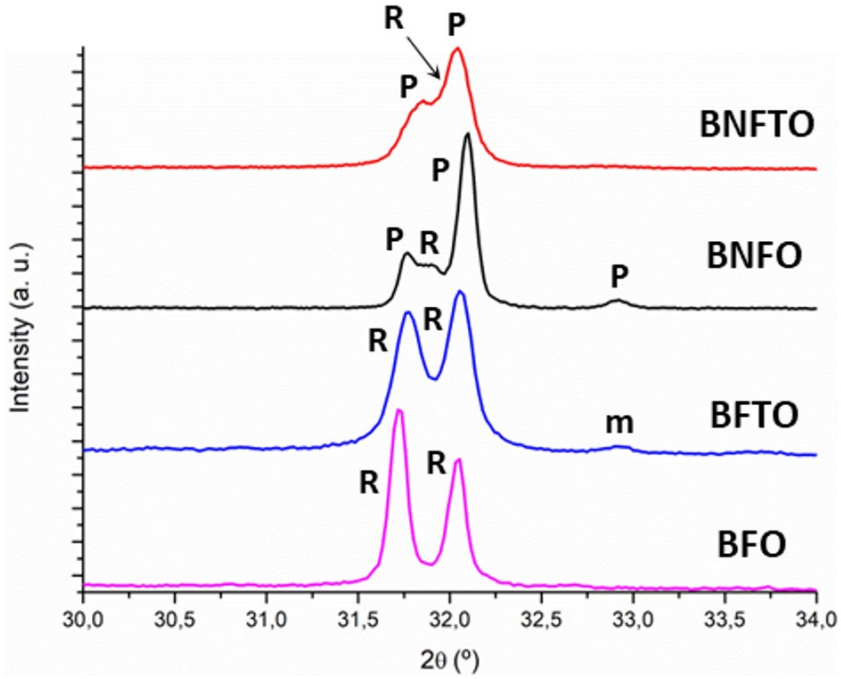

Figure 4. Evolution (decrease) of the rhombohedral distortion as a function of Nd-doping, see explanation in ext. R stands for the rhombohedral *R3c* phase and P for the orthorhombic *Pbam* phase of $BiFeO_3$; m indicates the presence of the mullite-type $Bi_4Fe_2O_9$ compound.

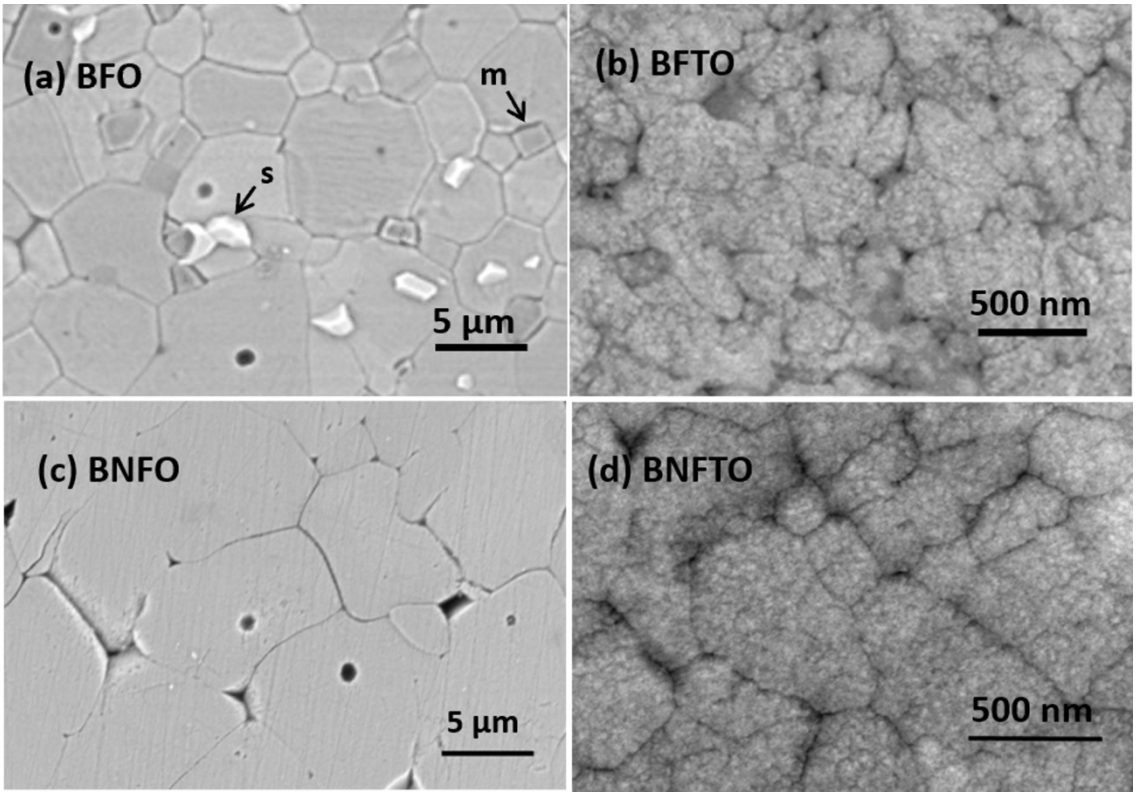

Figure 5.- FESEM micrographs taken on the etched surfaces of the four sintered compositions: (a) BFO sample sintered at 800 ºC/ 2 h, (b) BFTO sample sintered at 825 ºC/2 h, (c) BNFO sample sintered at 925 ºC/4 h and (d) BNFTO sample sintered at 925 ºC/8 h. s indicates the presence of the secondary $Bi_{25}FeO_{40}$ sillenite phase and m the presence of the secondary $Bi_4Fe_2O_9$ mullite grains.

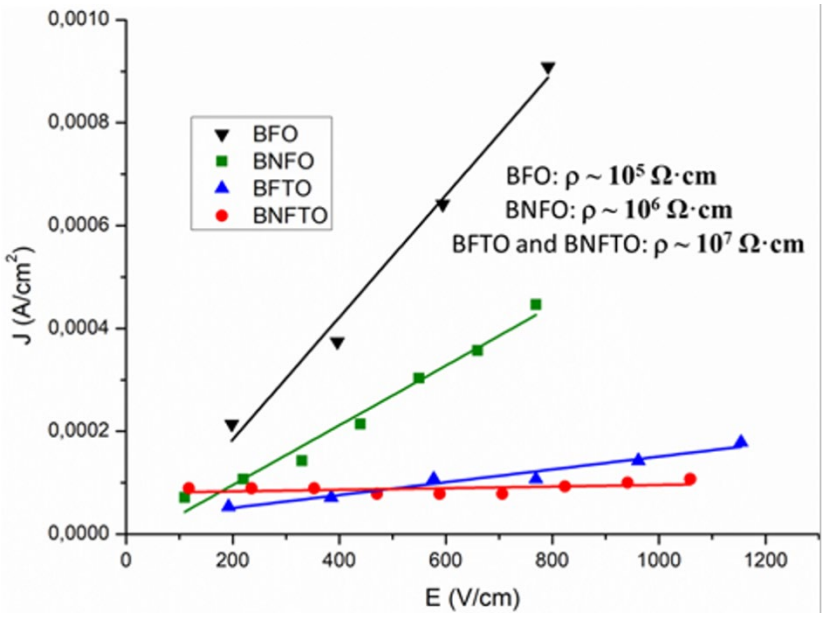

Figure 6. Current density as a function of the applied electric field for the four sintered materials.

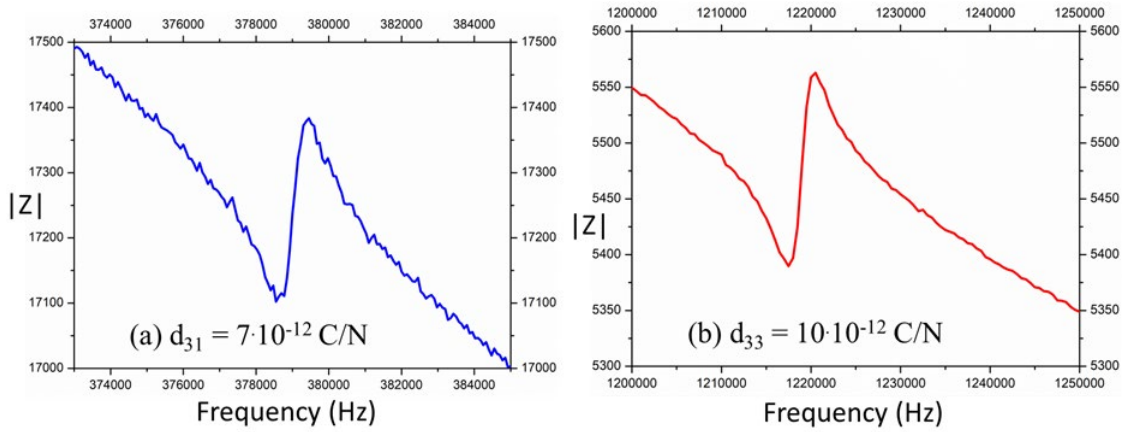

Figure 7. Piezoelectric coefficients (a) d_{31} and (b) d_{33} for the BNFTO sample as measured by the resonance-antiresonance methodology.

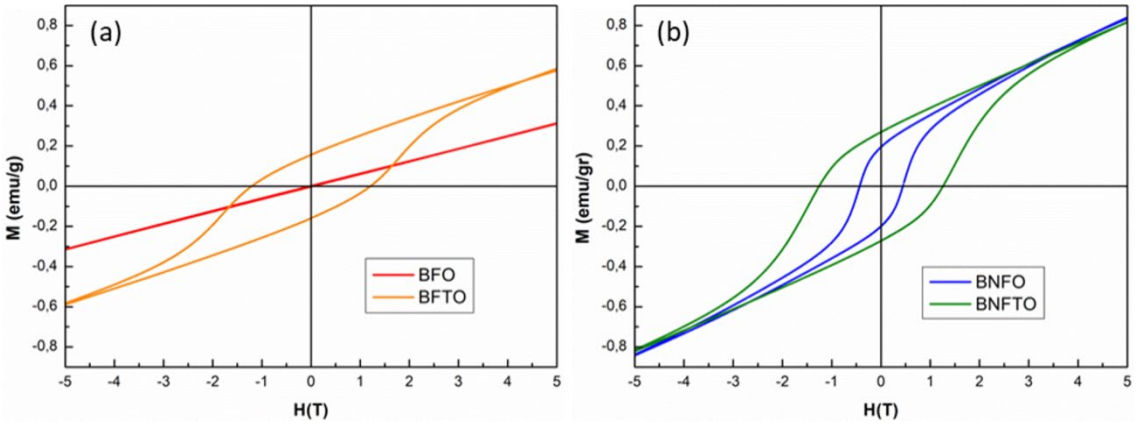

Figure 8. Room temperature magnetization curves for the (a) BFO and BFTO, and the (b) BNFO and BNFTO sintered samples.